Mesoporous Fe-doped TiO$_2$ sub-microspheres with enhanced photocatalytic activity under visible light illumination

Chin Jung Lin [a], Ya Hsuan Liou [b,*], Yichi Zhang [c], Chi Liang Chen [d], Chung-Li Dong [e], Szu-Ying Chen [b], Galen D. Stucky [c]

[a] Department of Environmental Engineering, National Ilan University, 1, Sec. 1, Shen-Lung Road, I-Lan 260, Taiwan
[b] Department of Geosciences, National Taiwan University, P.O. Box 13-318, Taipei 106, Taiwan
[c] Department of Chemistry and Biochemistry, University of California, Santa Barbara, CA 93106, United States
[d] Institute of Physics, Academia Sinica, Taipei 11529, Taiwan
[e] National Synchrotron Radiation Research Center (NSRRC), Hsinchu 30076, Taiwan

ARTICLE INFO

ABSTRACT

Mesoporous Fe-doped TiO$_2$ sub-microspheres (m-Fe-TMS) with high surface area, accessibility, and crystallinity were prepared using a rapid and continuous aerosol-assisted self-assembly (AASA) process for visible-light photocatalytic degradation of persistent pharmaceuticals. The results of X-ray absorption near-edge structure (XANEX) spectroscopy indicate that iron exists as octahedrally coordinated Fe^{3+} ions substituting Ti^{4+} in the TiO$_2$ lattice. The similarity of the Fe/Ti ratios in the bulk and on the surface, as determined by energy dispersive X-ray spectroscopy (EDX) and X-ray photoelectron spectroscopy (XPS), reveals that the substitution of Ti^{4+} by Fe^{3+} ions uniformly occurs within m-Fe-TMS. UV–vis diffuse reflectance spectroscopy shows that m-Fe-TMS exhibits a shift in the absorption threshold toward the visible spectrum. Under visible light irradiation, m-Fe-TMS exhibits a maximum rate of pharmaceutical photodegradation four times that of m-TMS. The photocatalytic degradation rates are reproducible with m-Fe-TMS, even after 10 repeated runs. The formation of chemical Fe—O—Ti bonds, and not of isolated Fe$_2$O$_3$ particles, leads to the inhibition of photocorrosion and leaching in the photocatalytic reactions. The ease and scalable production of m-Fe-TMS using the AASA process will facilitate the development of visible light-driven photocatalysts for decomposition of environmental contaminants.

1. Introduction

Considerable attention has been given to mesostructured metal oxides because of their potential use in energy- and environment-related fields [1–4]. Their effectiveness in practical applications varies with their mesoporosity, chemical composition, crystallinity, specific surface area, and most importantly, the morphology and texture of the material [5–7]. In this family of materials, mesoporous titania is of particular interest because it has a photoactive semiconductive framework with mesoporous channels that offer increased surface area and enhanced accessibility. However, limited by titania's low quantum efficiency and high band gap (3.0–3.2 eV) in the ultraviolet (UV) wavelength range, the use of mesoporous titania as highly active photocatalyst remains challenging to date.

Researchers have reported several approaches to resolve this intrinsic limitation, which include doping titania with either anions or metallic species or photosensitizing with organic dyes that are often efficient but unstable [8–12]. Doping with metallic species has been viewed as an effective way to lower the band gap of TiO$_2$ and to restrict the electron–hole recombination, thus enhancing the quantum efficiency [2,13–15]. A more intimate and conformal metallic dopant/TiO$_2$ junction is desired. That provides homogeneously doping within the titania framework while minimizing deposition at the channel entrances, thus allowing easy access of outer light and free diffusion of reactant molecules into the nanochannels.

The aerosol-assisted self-assembly (AASA) process obtains mesoporous sub-microspheres with high surface area and crystallinity through a continuous and large-scale production route. The first report on AASA was published in 1999 by Lu et al. [16], in which they prepared silica-based mesostructured spherical nanoparticles. Subsequently, non-silicate single-component materials, such as TiO$_2$, ZrO$_2$, and Al$_2$O$_3$ spheres, have become overwhelmingly dominant; they are produced using modified AASA [17–19]. However, the dissimilar hydrolysis and condensation behaviors of metal alkoxides make building mixed-metal oxide frameworks with AASA difficult. Stucky and co-workers [20] induced the growth of

* Corresponding author. Tel.: +886 2 33669861; fax: +886 2 23636095.
E-mail address: yhliou@ntu.edu.tw (Y.H. Liou).

metal oxoacetate ligands in the starting solution with the esterification of acetic acid to inhibit condensation of certain metal ions. A few multi-component spheres, such as CuO–TiO$_2$, Al–Si–O, and BaTiO$_2$, have been successfully fabricated.

In this work, we utilized AASA to substitutionally dope iron within the titania framework, wherein the surfactant, titania, and the iron building clusters were cooperatively assembled in a one-step process. The optical and electronic structural properties of the prepared samples were characterized by UV–vis diffuse reflectance spectroscopy (UV-Vis DRS), X-ray diffraction (XRD), X-ray photo-electron spectroscopy (XPS), and X-ray absorption near-edge structure (XANES) spectroscopy. Their morphological structure was also examined by field-emission scanning electron microscopy (FE-SEM), high-resolution transmission electron microscopy (HR-TEM), energy-dispersive X-ray spectroscopy (EDX), and N$_2$ sorption isotherms at 77 K. Paracetamol, a widely occurring human-derived pharmaceutical in the environment [21], was chosen as the target organic compound for the photocatalytic oxidation reactions. The photocatalytic activity of the mesoporous titania sub-microspheres with different iron contents was determined under visible-light illumination. Repeated experiments on the photocatalytic degradation of paracetamol in an acidic solution were also carried out to evaluate the durability of the prepared photocatalytic samples.

2. Experimental methods

2.1. Preparation of photocatalysts

The mesoporous TiO$_2$ (m-TMS) and mesoporous Fe-doped TiO$_2$ (m-Fe-TMS) sub-microspheres were prepared by AASA. A precursor solution of ethanol contained 1 Ti(OBu)$_4$:4 acetic acid:1.2 HCl:20 EtOH:0.01 F127 in molar ratio and iron ions were added with in concentrations ranging from 0% to 5.0%, relative to the Ti weight. The temperature of the furnace was kept at 400 °C during the spray process. The dry powder was collected using a 0.45 μm filter. These as-synthesized mesostructured hybrid spheres were then calcinated at 350 °C (ramp rate 1 °C/min) in air for 5 h.

2.2. Characterization of photocatalysts

The prepared m-TMS and m-Fe-TMS were characterized by UV-Vis DRS, XRD using Cu-Kα (λ = 1.54 Å) radiation, FE-SEM (JEOL JSM-7000F), and HR-TEM (JEOL JEM-2100). The XPS measurements were performed using a Vacuum Generators ECSALAB MKII photoelectron spectrometer (VG Co., East Grinstead, UK) with an ALKαX-ray source (1486.6 eV) and a hemispherical 150 mm mean radius electron analyzer having a takeoff angle of 90°. The binding energies of the photoelectrons were determined by assuming that the energies of the carbon 1s electrons were 284.5 eV. During data acquisition, the pressure in the sample chamber did not exceed 5×10^{-10} Torr. The Brunauer–Emmett–Teller (BET) surface areas of the prepared samples were obtained from N$_2$ sorption isotherms at liquid N$_2$ temperature using the Micrometrics ASAP 2010 analyzer. XANES spectroscopy measurements were used to identify the electronic structure on the Fermi level (unoccupied state) of prepared samples. XANES spectroscopy measurements were performed at

the National Synchrotron Radiation Research Center in Taiwan. The transition metal L-edge and the oxygen K-edge were recorded at the high-energy spherical grating monochromator BL20A1 beamline using the total electron yield mode, with a base pressure of 5×10^{-9} Torr and a resolving power of about $E/\Delta E = 8000$. Standard TiO$_2$ and Fe$_2$O$_3$ were used for energy calibration and for comparing the different electronic valence states and crystal symmetries.

2.3. Photocatalytic degradation of paracetamol

Paracetamol was used as a target compound to test the photo-catalytic activity of the prepared photocatalysts. The photocatalytic degradation of paracetamol was evaluated using a Rayonet RPR-100 Photoreactor equipped with sixteen visible-light lamps. The spectral response was with a maximum at 420 nm, a FWHM of about 15 nm and <5% of the intensity in the UV region. The mixture containing the photocatalysts in an aqueous solution of 50 mg/L paracetamol (25 mL) was magnetically stirred for 30 min in the dark before switching on the light. The concentration of the photocatalysts was 4.0 g/L.

2.4. Sample analysis

One milliliter of the aqueous solution was filtered using a Millipore filter (25 mm diameter, 0.2 μm pore size) and analyzed immediately. The paracetamol concentrations were measured using HPLC (Agilent; column, ZORBAX Eclipse XDB-C18, 4.6 mm × 150 mm, 5 μm) with a flow rate of 1.0 mL/min and UV absorbance detection at 245 nm. The mobile phase was 25% methanol and 75% miniQ water. The injection volume was 10 μL. Each experiment was performed in triplicate, and all results were expressed as a mean value of the three experiments.

3. Results and discussion

3.1. Surface morphologies

Fig. 1a shows a typical SEM image of the m-0.5Fe-TMS prepared using the AASA process. The average size of the spheres is ~1 μm, and they are free of surface cracks and intersphere adherence. The as-prepared spheres have very smooth surfaces without obvious granular features (Fig. 1a). After calcinated at 350 °C for 5 h in air, spheres with comparatively rough surfaces were produced (Fig. 1b). As illustrated by the high-magnification SEM image (Fig. 1b), pores could be observed over the surface of the TiO$_2$ sphere. The uniform pore size distribution and close packing configuration of the TiO$_2$ spheres are clearly shown in the HR-TEM images (Fig. 1c). The high crystallinity is confirmed by the clear lattices, as shown in the inset of Fig. 1c. The EDX spectrum of the m-0.5Fe-TMS is shown in Fig. 1d, which was carried out under HR-TEM. The characteristic peaks in the spectrum are associated with Ti, O, and Fe. Quantitative analysis reveals that the weight ratio of Fe and Ti is close to 0.5, which is equal to what was distributed in the precursor solution. The nitrogen adsorption measurements demonstrate that all the materials exhibit the type IV isotherm behavior, with high BET surface areas ranging from 116 m^2 g^{-1} to 144 m^2 g^{-1} (Table 1; see also

Table 1
The BET surface area, pore size and pore volume of the prepared photocatalysts; and their observed pseudo-first-order reaction rate constants.

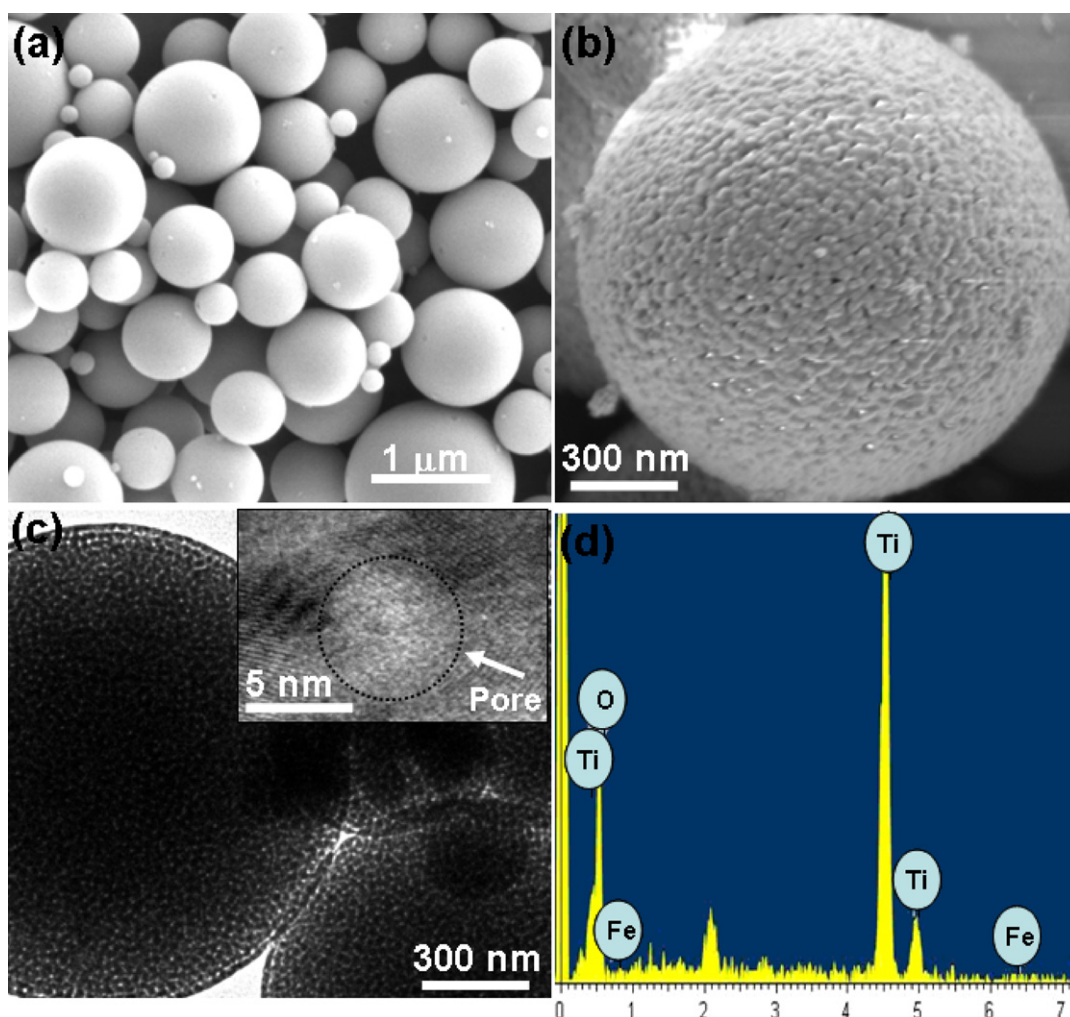| Photocatalyst	BET surface area (m^2 g^{-1})	Pore size (nm)	Pore volume (cm^3 g^{-1})	k_{obs} (10^{-3} min^{-1})	r^2
m-TMS	144	7.3	0.25	6.7 ± 0.2	0.998
m-0.1Fe-TMS	120	5.7	0.17	9.2 ± 0.3	0.998
m-0.5Fe-TMS	116	6.2	0.18	25.5 ± 0.5	0.977
m-1.0Fe-TMS	117	5.7	0.16	9.6 ± 0.3	0.998
m-5.0Fe-TMS	117	5.9	0.17	3.8 ± 0.1	0.937

Fig. 1. (a) SEM image of the as-prepared m-0.5Fe-TMS; (b) SEM image; (c) low-magnification HR-TEM image and (d) the EDX spectrum of m-0.5Fe-TMS calcined at 350 °C. The inset in (c) is high-magnification HR-TEM image.

Supplementary information, Fig. S1). The Barrett–Joyner–Halenda (BJH) pore sizes, determined from the adsorption branches, are approximately 3–5 nm, consistent with HR-TEM characterization.

3.2. Structural characterizations

Fig. 2 shows the XRD patterns of m-0.1Fe-TMS, m-0.5Fe-TMS, m-1.0Fe-TMS, and m-5.0Fe-TMS. All the samples possess the anatase phase of TiO_2 (JCPDS 21-1272). The observed peaks at 2θ of 25.3°, 37.8°, 48.0°, 53.8°, and 54.9° represent the diffraction of the (1 0 1), (0 0 4), (2 0 0), (1 0 5), and (2 1 1) crystal planes, respectively. This finding indicates that an attractive feature of our fabrication process for the mesoporous spheres is the facile creation of nanocrystal domain frameworks at relatively low calcination temperatures. No typical refractions of the iron oxide phases, such as Fe_2TiO_5 or Fe_2O_3, are observed. However, differences still exist among the iron oxides. With increasing Fe content, the peaks slightly broaden and the crystallite sizes are reduced, indicating a slight distortion in the crystal structure. This result may be attributed to the formation of crystallographic point defects due to the substitution of Ti^{4+} by Fe^{3+} ions. Most iron ions might be inserted into the structures of TiO_2 located at the interstices, or might occupy some of the titanium lattice sites to form a solution with iron–titanium solids.

The UV–vis diffuse reflectance spectra of the m-TMS, m-0.1Fe-TMS, m-0.5Fe-TMS, m-1.0Fe-TMS, and m-5.0Fe-TMS are given in

Fig. 3. The band gap adsorption edge of m-TMS is approximately 400 nm, which does not exhibit noticeable adsorption in the visible regime. All the m-Fe-TMS samples, however, exhibit a red shift of the absorption edge. With increasing Fe content, the m-Fe-TMS
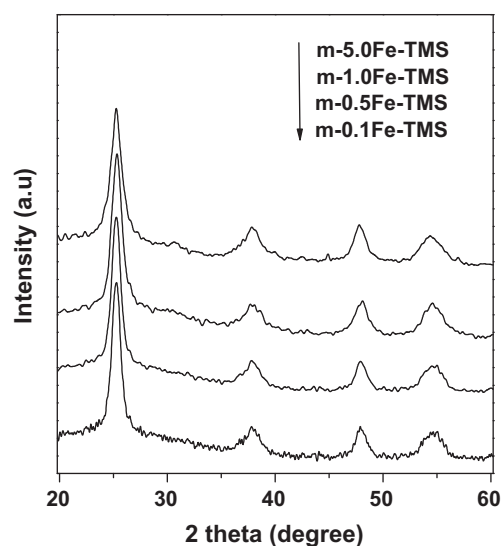

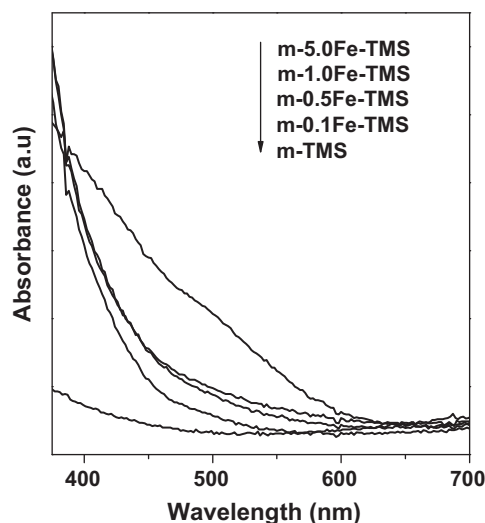**Fig. 2.** XRD patterns of m-0.1Fe-TMS, m-0.5Fe-TMS, m-1.0Fe-TMS, and m-5.0Fe-TMS, respectively.

Fig. 3. UV–vis spectra of m-TMS, m-0.1Fe-TMS, m-0.5Fe-TMS, m-1.0Fe-TMS, m-5.0Fe-TMS.

Fig. 5. (a) Ti $L_{3,2}$-edge ($2p_{3/2,1/2} \rightarrow 3d$ transition) XANES spectra of m-TMS, m-0.5Fe-TMS, m-1.0Fe-TMS, m-5.0Fe-TMS, and standard TiO$_2$ (anatase and rutile crystalline phases) and (b) Fe L_3-edge($2p_{3/2} \rightarrow 3d$ transition) spectra.

samples present an enhancement of the light absorption in the visible range, with the color of the samples changing from white to yellow. Metal-doping introduces electronic states into the band-gap of TiO$_2$ that are spread across the said band-gap [22,23]. Therefore, the red shift of the absorption edge for the m-Fe-TMS samples might come from the transition of the excitation of 3d electrons from the ferric ions to the conduction band of TiO$_2$. The observed enhanced visible light absorbance is expected to considerably increase the utilization of visible light for photocatalytic reactions.

The XPS spectra of m-TMS and m-0.5Fe-TMS are shown in Fig. 4. The Ti $2p_{3/2}$ and Ti $2p_{1/2}$ spin–orbital-splitting photoelectrons for m-0.5Fe-TMS are located at 459.4 and 465.2 eV, respectively. The small binding energy shifts to higher energies compared with the ones in the undoped TiO$_2$ (459.1 and 464.9 eV, respectively). This finding may be attributed to the formation of the Fe—O—Ti bonds in the crystal lattice [24]. The O 1s binding energy of m-0.5Fe-TMS is located at a higher energy than 530.9 eV, corresponding to the value in m-TMS assigned to the metallic oxide (O^{2-}) in the TiO$_2$ lattice. A high-resolution spectrum of the Fe 2p region for m-0.5Fe-TMS is shown in Fig. 4c. The spectrum indicates the existence of the doublet Fe $2p_{3/2}$ and Fe $2p_{1/2}$ with weak satellite, whereas typical Fe$_2$O$_3$ oxides possess significant satellite structures on the high-binding energy side [25,26]. The binding energies within the range 710.4–712.3 eV are assigned to Fe $2p_{3/2}$ of the Fe^{3+} cation. The
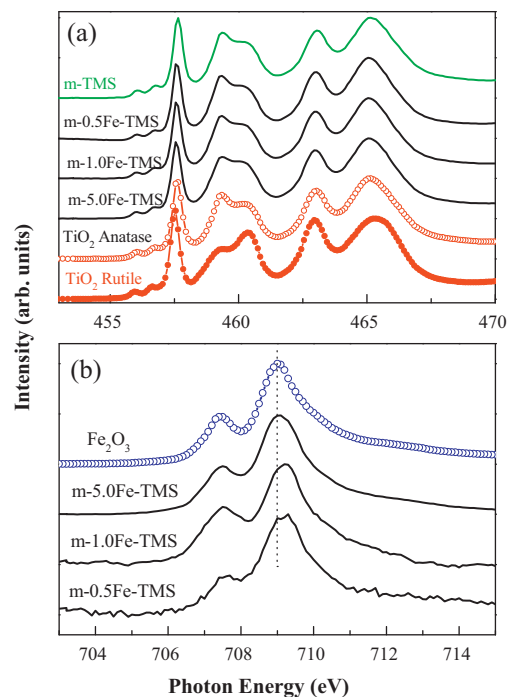
results indicate that the Fe^{3+} cations penetrate into the TiO$_2$ lattice and substitute the Ti^{4+} cations, such that substitutional doping of Fe^{3+} occurs. The Fe/Ti weight ratio was estimated to be 0.47 by XPS. The similarity of the XPS and EDS results reveals that the substitution of Ti^{4+} by Fe^{3+} ions uniformly occurs within m-0.5Fe-TMS. The formation of the new Fe—O—Ti bonds in the crystal lattice changes the electron densities of the Ti^{4+} cations and the O^{2-} anions, causing a subsequent change in the charge distribution of the atoms on the photocatalyst surface, which may then enhance the photocatalytic activity.

The XANES spectra at the Ti $L_{3,2}$-edges of m-0.5Fe-TMS, m-1.0Fe-TMS, and m-5.0Fe-TMS, along with reference samples of TiO$_2$ (anatase and rutile crystalline phases), are presented in Fig. 5a. The line shapes of all the m-Fe-TMS spectra are similar to those of anatase TiO$_2$, which is consistent with XRD results. This finding implies that Ti ions are quadricvalance in m-Fe-TMS and its phase remains anatase as Fe is doped into the TiO$_2$ lattice. The
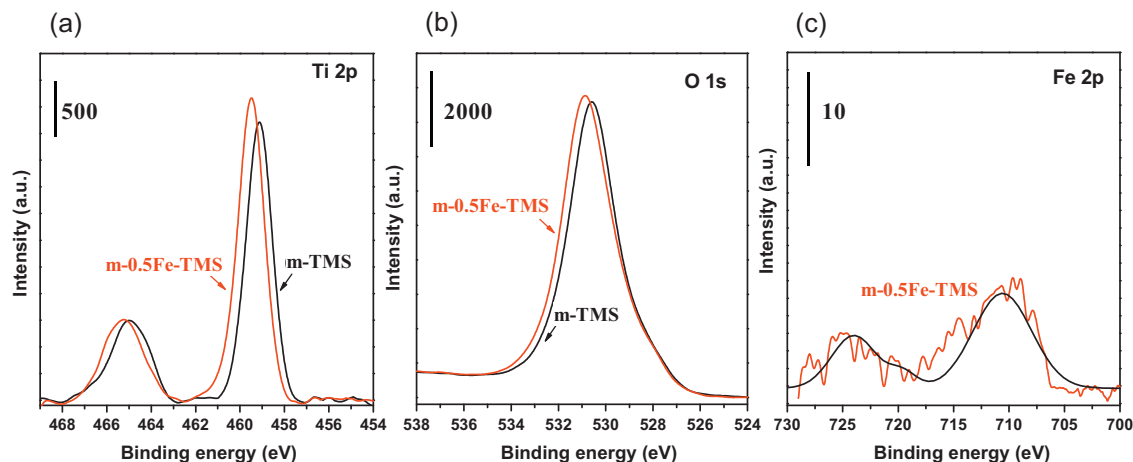

Fig. 4. High-resolution XPS spectra from the surface of m-TMS and m-0.5Fe-TMS: (a) Ti 2p, (b) O 1s, and (c) Fe 2p.

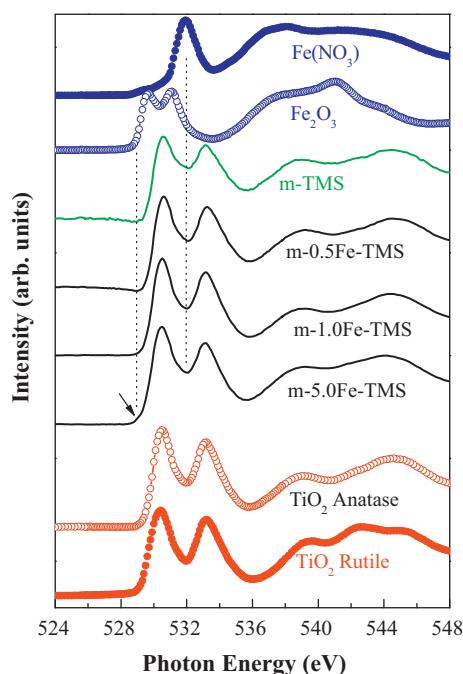Fig. 6. O K-edge XANES spectra of m-TMS, m-0.5Fe-TMS, m-1.0Fe-TMS, m-5.0Fe-TMS and standards.

Fig. 7. Photocatalytic degradation of 50 mg/L of paracetamol by m-TMS and m-Fe-TMS under visible light illumination (λ_{max} = 420 nm). m-0.5Fe-TMS for the dark adsorption test. Errors present 95% confidence intervals.

modification of the e_g band in the spectrum is an indication of the distorted octahedral lattice that is also observed in the Ti K-edge XAS (Fig. S2). The Fe L_3-edge XANES spectra are presented in Fig. 5b. Both the spectral profile and the peak positions of m-5.0Fe-TMS are found to be very similar to those of Fe_2O_3. However, the spectrum of m-0.5Fe-TMS, although similar, is different from that of Fe_2O_3 by the shift to higher photon energy levels. In the m-1.0Fe-TMS sample, the main peak has a similar energy to the m-0.5Fe-TMS sample, but a broader shoulder feature is seen. Fig. 6 shows the near-edge features of the O K-edge spectra. Upon close inspection of the spectral line shape of m-TMS, the pre-peak features are broader than those in the bulk TiO_2 (anatase). This broadening may be due to the presence of defects, which is generally expected to increase the bandwidth. As Fe is doped into m-TMS, the dopant may occupy the defect and the structure may become stabilized. Thus, a narrower bandwidth in m-Fe-TMS than that in m-TMS is observed. The onset of the absorption energy of m-5.0Fe-TMS shifts to low energy compared with m-0.5Fe-TMS, and has nearly the same onset energy as Fe_2O_3. Therefore, according to the XAS results, the formation of Fe—O—Ti bond is expected upon 0.5 wt% Fe doping. As the Fe concentration is increased, both the spectral profile and the peak position gradually match those in Fe_2O_3. The m-1.0Fe-TMS sample exhibits the mixed states of both m-0.5Fe-TMS and Fe_2O_3. The m-5.0Fe-TMS resembles that of Fe_2O_3, indicating Fe is overdoped and iron oxides is presented.

3.3. Photocatalytic degradation of paracetamol

Fig. 7 shows the degradation kinetics of the paracetamol solution at 25 °C and pH 5.5. Direct photolysis in the control experiment shows that no significant decrease in the concentration of paracetamol solution occurs in the absence of m-TMS and m-Fe-TMS. This finding indicates the photostability of paracetamol under visible light within an irradiation period of 6 h. The reactions were then conducted under dark conditions, and no reactions were observed even after 6 h. A first-order rate model, Eq. (1), effectively describes
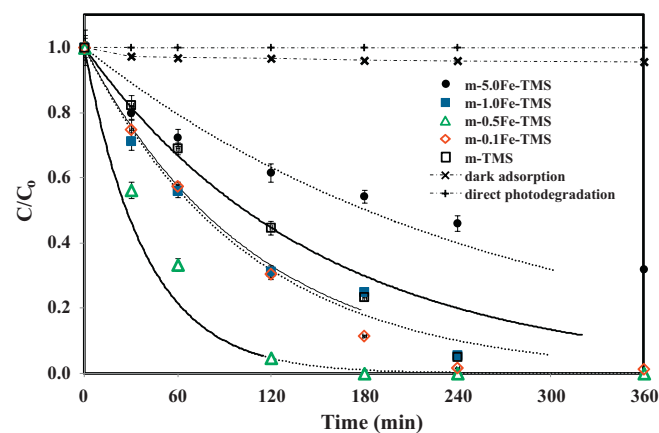
the photocatalytic degradation of the paracetamol solution as follows:

$$\frac{-dC}{dt} = k_{obs}C \tag{1}$$

where C refers to the concentration of paracetamol, t is the reaction time (min), and k_{obs} is the observed rate constant (min^{-1}). The resulting value of k_{obs} is $(6.7 \pm 0.2) \times 10^{-3}$ min^{-1} for m-TMS, which is higher than 0.0062 for the Degauss P25 TiO_2 (see Fig. S3). The influence of increasing the Fe dopant on m-Fe-TMS is also depicted in Fig. 7. The values of k_{obs} are $(9.2 \pm 0.3) \times 10^{-3}$ min^{-1}, $(25.5 \pm 0.5) \times 10^{-3}$ min^{-1}, $(9.6 \pm 0.3) \times 10^{-3}$ min^{-1}, and $(3.8 \pm 0.1) \times 10^{-3}$ min^{-1} for m-0.1Fe-TMS, m-0.5Fe-TMS, m-1.0Fe-TMS, and m-5.0Fe-TMS samples, respectively. The influence of doping Fe on the k_{obs} value exhibits a volcano curve and reaches a maximum value over m-0.5Fe-TMS (Fig. 8). However, when Fe/Ti is increased to 1.0%, a significant drop in k_{obs} value is observed. Obviously, the 32% paracetamol concentration that remained after 6 h of the reaction resulted from the reduced photocatalytic activity of m-5.0Fe-TMS. Thus, a higher photocatalytic activity for the degradation of paracetamol is obtained for m-Fe-TMS compared with that of m-TMS. The high photocatalytic activity of the samples with low Fe dopant arises from the fact that Fe^{3+}-doping introduces vacancies in the TiO_2 lattice and lowers the valence band maximum. This phenomenon has also been observed by other groups [13,27]. A very high Fe dopant
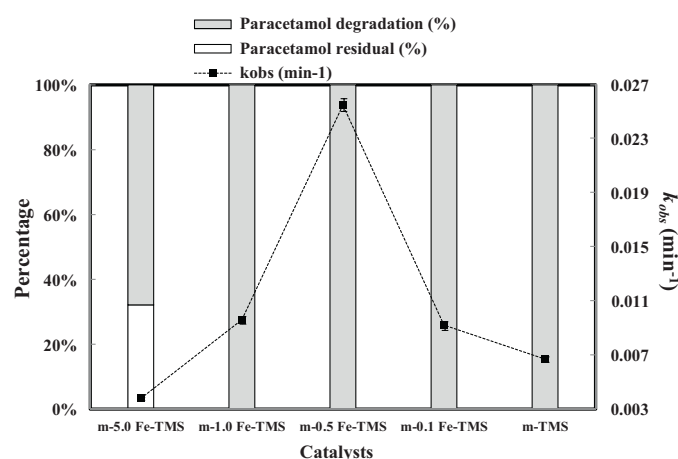

Fig. 8. Paracetamol degradation and residual percentage, and k_{obs} in dependence of different Fe doped catalysts.
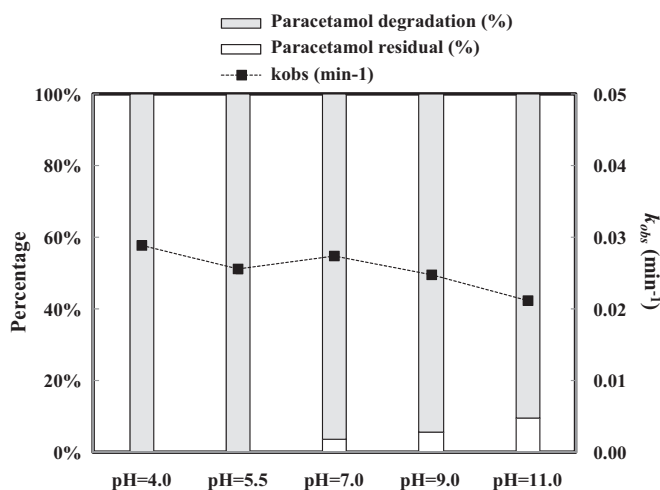
Fig. 9. Paracetamol degradation and residual percentage, and k_{obs} with m-0.5Fe-TMS at 360 min in dependence of the pH value.

Fig. 10. Repeated photodegradation of paracetamol by m-0.5Fe-TMS under visible light illumination (λ_{max} = 420 nm). Errors present 95% confidence intervals.

would generate isolated Fe_2O_3 particles expelled from the m-Fe-TMS framework to the pore channels. The Fe_2O_3 particles may act as centers of charge recombination and slow down mass transport within the channels, thus reducing the degradation rate. In this study, some aromatic compounds and carboxylic acids were determined by GC/MS and HPLC as the reaction intermediates (see Table S1), which exhibited that hydroxylation through OH$^\bullet$ addition onto the aromatic rings followed by further oxidation. Further mineralization eventually yielded ammonium and small amount of nitrate. This result is consist with the reaction pathways reported by Yang et al. [30] during the photocatalytic degradation of paracetamol. As compared to m-TMS, the amount of intermediates was slight increased with doping Fe in which no accumulation of intermediates was observed in the m-0.5Fe-TMS system. This indicates that photocatalytic degradation of paracetamol with m-Fe-TMS under visible-light irradiation is potentially a feasible treatment process.

The pH dependence of the paracetamol removal photoactivity for m-0.5Fe-TMS was examined over the range of pH from 4.0 to 11.0. In Fig. 9, the k_{obs} values of paracetamol photodegradation at a pH of 4.0, 5.5, 7.0, 9.0, and 11.0 are $(28.8 \pm 0.3) \times 10^{-3}$ min^{-1}, $(25.5 \pm 0.5) \times 10^{-3}$ min^{-1}, $(27.4 \pm 0.4) \times 10^{-3}$ min^{-1}, $(24.8 \pm 0.5) \times 10^{-3}$ min^{-1}, and $(21.1 \pm 0.4) \times 10^{-3}$ min^{-1}, respectively. A slightly negative effect of high pH values on the k_{obs} value was observed, in which the values drop at pH > 9. The remaining paracetamol concentration increases with an increase in the pH value. The solution pH might change the band edge position or surface charge of the photocatalyst. Paracetamol is negatively charged at pH > 9.5 [28]. Thus, the electrostatic repulsion between the prepared m-0.5Fe-TiO$_2$ surface and paracetamol gradually increases with increasing pH, and further degradation reduces the already poor adsorption of paracetamol. Besides, H$^+$ ions facilitate the capture of photogenerated electrons by Fe^{3+} ions to enhance the oxidation reaction of the target contaminants [29]. Hence, it is not surprising that the degradation rate of paracetamol is better in the acidic solution.

3.4. Durability of the photocatalyst

Ten repeated experiments for the photocatalytic degradation of paracetamol at pH 5.5 using m-0.5Fe-TMS for 240 min were carried out under 420 nm illumination to ensure the possibility of recycling the used mesoporous Fe-doped TiO$_2$ sub-microspheres. At the end of ea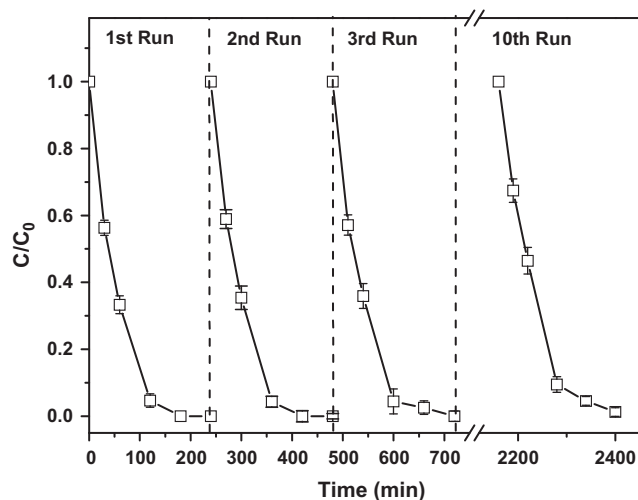ch run, m-0.5Fe-TMS was collected with centrifugal sedimentation and then the solution was discarded and replaced with another fresh solution with 50 mg/L paracetamol solution (pH 5.5), as seen in Fig. 10. The results show that the photocatalytic degradation efficiency remains fairly consistent throughout the 10 repetitive experiments. Fig. S4 shows the XPS spectra of O 1s, Ti 2p, and Fe 2p of m-0.5Fe-TMS before and after the 10 repeated runs. There was no noticeable difference in the XPS spectra of m-0.5Fe-TMS, indicating that the substitutional Fe-dopant in TiO$_2$ framework is neither reduced nor oxidized during the photocatalytic reaction. Moreover, the leaching of Fe is not observed, as confirmed by inductively coupled plasma optical emission spectroscopy (data not shown). The strong durability of the photocatalysts may originate from the suppression of photocorrosion and leaching in the photocatalytic reactions due to the formation of chemical Fe–O–Ti bonds, and not of isolated Fe_2O_3 particles.

4. Conclusions

We have prepared high-surface-area, crystalline mesoporous Fe-doped TiO$_2$ sub-microspheres that are efficient visible-light-sensitive photocatalysts using rapid and continuous aerosol-assisted self-assembly. The achieved high photocatalytic activity for paracetamol degradation under visible irradiation was attributed to the strong absorption within the visible spectrum and the effective decrease in charge recombination in the TiO$_2$ lattice, which were introduced by substitutional Fe^{3+} doping. The strong interactions between Fe and TiO$_2$ may be formed from some features of AASA for the mesoporous spheres including (1) the growth of metal oxoacetate ligands in the starting solution to inhibit the dissimilar hydrolysis and condensation behaviors of metallic ions. (2) The facile creation of nanocrystal domain frameworks at relatively low temperatures. The structure of the Fe–O–Ti bond was photochemically stable and leaching of Fe was not observed, resulting in the strong durability of the photocatalyst. Other metal dopants could also be encapsulated in the mesoporous TiO$_2$ sub-microspheres. AASA supplies a new approach for designing powerful multicomponent mesoporous spherical catalysts.

Appendix A. Supplementary data

Supplementary data associated with this article can be found, in the online version, at http://dx.doi.org/10.1016/j.apcatb.2012.08.011.

References

[1] M.H. Bartl, S.W. Boettcher, K.L. Frindell, G.D. Stucky, Accounts of Chemical Research 38 (2005) 263–271.
[2] H.X. Li, Z.F. Bian, J. Zhu, Y. Huo, H. Li, Y. Lu, Journal of the American Chemical Society 129 (2007) 4538–4539.
[3] H.-J. Koo, Y.J. Kim, Y.H. Lee, W.I. Lee, K. Kim, N.-G. Park, Advanced Materials 20 (2008) 195–199.
[4] S.S. Thind, G. Wu, A. Chen, Applied Catalysis B: Environmental 111–112 (2012) 38–45.
[5] B.Z. Tian, X.Y. Liu, B. Tu, C.Z. Yu, J. Fan, L.M. Wang, S.H. Xie, G.D. Stucky, D.Y. Zhao, Nature Materials 2 (2003) 159–163.
[6] H. Li, Z. Bian, J. Zhu, D. Zhang, G. Li, Y. Huo, H. Li, Y. Lu, Journal of the American Chemical Society 129 (2007) 8406–8407.
[7] J. Lee, M.C. Orilall, S.C. Warren, M. Kamperman, F.J. Disalvo, U. Wiesner, Nature Materials 7 (2008) 222–228.
[8] J. Cao, J.Z. Sun, J. Hong, X.G. Yang, H.Z. Chen, M. Wang, Applied Physics Letters 83 (2003) 1896–1898.
[9] C. Kim, J. Choi, Y.B. Lee, J.H. Hong, J.I. Lee, J.W. Yang, W.I. Lee, N.H. Hur, Chemical Communications (2006) 5024–5026 (Cambridge).
[10] I. Robel, M. Kuno, P.V. Kamat, Journal of the American Chemical Society 129 (2007) 4136–4137.
[11] Y. Mizukoshi, N. Ohtsu, S. Semboshi, N. Masahashi, Applied Catalysis B 91 (2009) 152–156.
[12] G.-S. Shao, F.-Y. Wang, T.-Z. Ren, Y. Liu, Z.Y. Yuan, Applied Catalysis B: Environmental 92 (2009) 61–67.
[13] W.Y. Teoh, R. Amal, L. Mädler, S.E. Pratsinis, Catalysis Today 120 (2007) 203–213.
[14] L. Cui, Y. Wang, M. Niu, G. Chen, Y. Cheng, Journal of Solid State Chemistry 182 (2009) 2785–2790.
[15] Z. Bian, J. Zhu, F. Cao, Y. Lu, H. Li, Chemical Communications (2009) 3789–3791.
[16] Y. Lu, H. Fan, A. Stumo, T.L. Ward, T. Rieker, C.J. Brinker, Nature 398 (1999) 223–226.
[17] D. Grosso, G.J.A.A. Soler Illia, E.L. Crepaldi, B. Charleux, C. Sanchez, Advanced Functional Materials 13 (2003) 37–42.
[18] A. Dong, N. Ren, Y. Tang, Y. Wang, Y. Zhang, W. Hua, Z. Gao, Journal of the American Chemical Society 125 (2003) 4976–4977.
[19] C. Boissière, L. Nicole, C. Gervais, F. Babonneau, M. Antonietti, H. Amenitsch, C. Sanchez, D. Grosso, Chemistry of Materials 18 (2006) 5238–5243.
[20] C.-K. Tsung, J. Fan, N. Zheng, Q. Shi, A.J. Forman, J. Wang, G.D. Stucky, Angewandte Chemie International Edition 47 (2008) 8682–8686.
[21] N.M. Vieno, T. Tuhkanen, L. Kronberg, Environmental Science and Technology 39 (2005) 8220–8226.
[22] Y.A. Cao, W.S. Yang, W.F. Zhang, G.Z. Liu, P. Yue, New Journal of Chemistry 28 (2004) 218–222.
[23] X.Z. Li, F.B. Li, Environmental Science and Technology 35 (2001) 2381–2387.
[24] R. Wang, R. Sakai, A. Fujishima, T. Watanabe, K. Hashimoto, Journal of Physical Chemistry B 103 (1999) 2188–2194.
[25] L. Dghoughi, B. Elidrissi, C. Bernède, M. Addou, M.A. Lamrani, M. Regragui, H. Erguig, Applied Surface Science 253 (2006) 1823–1829.
[26] F. Gracia, J.P. Holgado, F. Yubero, A.R. González-Elipe, Surface and Coatings Technology 552 (2002) 158–159.
[27] Y.-F. Tu, S.-Y. Huang, J.-P. Sang, X.-W. Zou, Materials Research Bulletin 45 (2010) 224–229.
[28] M. Brunner, A. Schmiedberger, R. Schmid, D. Jager, E. Piegler, H.G. Eichler, M. Muller, British Journal of Clinical Pharmacology 46 (1998) 425–431.
[29] H. An, J. Li, J. Zhou, K. Li, B. Zhu, W. Huang, Journal of Materials Chemistry 26 (2010) 603–610.
[30] L. Yang, L. Yu, M. Ray, Environmental Science & Technology 43 (2009) 460–465.